Transactions of the Indian National Academy of Engineering (2020) 5:555–571
https://doi.org/10.1007/s41403-020-00095-w

ORIGINAL ARTICLE

Comprehensive Assessment of Low Cycle Fatigue Behavior of Nickel-Base Superalloy Superni 263 in the Range 298–1023 K

Jhansi Jadav[1] · K. V. Rajulapati[1] · K. Bhanu Sankara Rao[2] · N. Eswara Prasad[3] · R. Mythili[4] · Kartik Prasad[5]

Received: 18 March 2020 / Accepted: 18 April 2020 / Published online: 8 May 2020

Abstract

The effects of temperature on low cycle fatigue (LCF) behavior of Superni 263 superalloy in the solution annealed plus aged state were examined between 298 and 1023 K. The initial microstructure consisted of intragranular spherical γ' (22 nm), intergranular $M_{23}C_6$ carbides and a few un-dissolved primary MC particles. Strain-controlled LCF tests were performed at a strain rate of 10^{-3} s^{-1}. Correlations between the initial microstructure, macroscopic cyclic deformation, fatigue life, crack initiation and propagation modes, evolving deformation substructure and phase changes have been attempted. Cyclic stress response displayed a marked variation in its temperature dependence. In general, the alloy exhibited initial hardening followed by very slight softening up to 473 K, continuous hardening to a maximum stress in between 573 and 873 K, and initial hardening succeeded by rapid softening at and above 923 K. Dynamic Strain Ageing (DSA) was noticed during 573–923 K. In the DSA domain, the alloy exhibited pronounced cyclic hardening at 673 K, displayed planar slip, stacking faults, high dislocation density and shearing of γ'. The macroscopic features revealed serrated flow in the plastic deformation portions of stress–strain hysteresis loops and inverse temperature dependence of maximum stress and inelastic strain generated at half-life. Fresh precipitation of γ' occurred at 973 K and 1023 K during LCF testing while prior existing γ' coarsened marginally above 923 K. The operating deformation mechanisms of γ' were identified and correlated with microscopic and macroscopic aspects. LCF life displayed a maximum at ~ 473 K and the reduction in life above 473 K was attributed to the deleterious effects of DSA and oxidation.

Keywords Superalloy · Superni 263 · Low cycle fatigue · Dynamic strain aging · Oxidation effects · Aero engine · Advanced ultra-supercritical plants

Introduction

The age-hardenable wrought Ni-based superalloy, Alloy 263, is based upon Ni–Co–Cr austenitic matrix. It is strengthened by combined effects of solid solution hardening and by the precipitation hardening associated with intragranular γ' [$Ni_3(Ti, Al)$] and intergranular $M_{23}C_6$, which precipitate on ageing at elevated temperatures. Solid solution elements such as Mo contribute to the strengthening of the alloy at elevated temperatures as a result of lattice distortion arising from atomic size differences (Smith et al. 2010). The benefits arising from solid solution strengthening elements comprises reduced diffusion and the lowering of stacking fault energy (Gianfrancesco 2017). This alloy is being used very extensively in aero-engines for various stationary components that include combustion chamber, casing, liner, exhaust ducting and bearing housing (Zhang and Knowles 2000). With increasing operating temperatures of gas turbines, the combustor and transition pieces are exposed to temperatures approximately in the range 973–1073 K. The usage of this alloy in aero-engine applications is primarily attributed to its low sensitivity to segregation, remarkable combination of high workability, weldability and resistance

✉ K. V. Rajulapati
kvrse@uohyd.ernet.in; kvrse.uoh@gmail.com

[1] School of Engineering Sciences and Technology, University of Hyderabad, Hyderabad 500046, India

[2] Pratt & Whitney Chair, University of Hyderabad, Hyderabad 500046, India

[3] Defence Materials Stores R&D Establishment, Kanpur 208013, India

[4] Indira Gandhi Centre for Atomic Research, Kalpakkam 603102, India

[5] Defence Metallurgical Research Laboratory, Hyderabad 500058, India

to creep on prolonged exposure to elevated temperatures up to 1023 K. Presently, the alloy is also under consideration for the forged thick-section rotor, superheater and reheater tubing of the steam generator of the advanced ultra-supercritical (A-USC) plants that are being designed to operate at ~ 993/1013 K with an applied stress of 310 kg/cm^2. In the past, investigations on Alloy 263 have been performed in order to (i) optimize the chemical composition that can ensure the microstructural stability by eliminating the brittle eta-phase precipitation at 1023 K, (ii) establish the melting route for production of industrial casts, (iii) manufacturing of thick-section and large diameter rotor and (iv) development of welding technologies for rotors and specification of post-weld heat treatment cycles (Zhang and Knowles 2000). Alloy 263 possessed minimum desired creep rupture strength of 100 MPa at 10^5 h in the range 1023–1033 K, making it a promising alloy for various components in A-USC plants (Maile 2013). Many thick-section components in A-USC power plant can be subjected to repeated thermal stresses as a result of temperature gradients resulting from start-ups and shut-downs as well as power transients. In order to ensure satisfactory performance, resistance to LCF has to be taken into consideration by the designer. Though some studies addressed on few aspects of LCF, thermal fatigue and creep–fatigue interaction behavior of Alloy 263 (Xie et al. 2011; Bhattachar 1995; Ratna and Sarma 1993; Pohja et al. 2015; Sahu et al. 2015), there are no systematic investigations on the effects of temperature on macroscopic and microscopic aspects of cyclic deformation, fracture modes and the micro-mechanisms influencing deformation and fracture in the solution annealed plus aged conditions. This investigation has been pursued to understand the role of dynamic strain aging and other temperature-dependent phenomena on strain-controlled cyclic deformation and fatigue life in the range 298–1023 K.

Experimental Details

The Alloy 263 was produced in India by M/s Mishra Dhatu Nigam Limited, Hyderabad under the trade name Superni 263 and was supplied in the form of 70 mm-diameter rolled bars, whose chemical composition (in Wt.%) is given in Table 1.

Table 1 Chemical composition of Superni 263 superalloy

Element	Wt.%	Element	Wt.%
C	0.074	N	0.005
Cr	20.00	Mn	0.400
Co	19.30	Si	0.030
Mo	05.90	Ag	0.0003
Ti	02.10	B	0.0050
Al	0.510	Bi	0.0005
P	0.005	Pb	0.0002
Fe	0.050	S	0.005
O	0.0012	Cu	0.020
Ni	Balance		

Blanks of 15 mm diameter were machined from 70 mm diameter rods by electro discharge machining. These blanks were subjected to a solution annealing treatment at 1373 K/90 min followed by water quenching and then aged at 1073 K/8 h. The 15-mm parallel gauge length and 6.35 mm gauge diameter LCF specimens were machined from the heat-treated blanks, and the details of the specimen design are given in (Jadav 2019). Fully reversed, total axial strain-controlled LCF tests, employing triangular waveform, were performed in air at various temperatures in the range 298–1023 K at a total strain amplitude of ± 0.60% and a strain rate of 10^{-3} s^{-1}. The stress–strain hysteresis loops were recorded continuously to obtain the information on cycle-dependent changes in stress and inelastic strain amplitude. All the tests were conducted according to ASTM E-606 standard, using MTS 880 closed loop servo-hydraulic testing system of ± 100 kN dynamic load capacity that is equipped with resistance heating facility. During the LCF test, the temperature was maintained within an accuracy of ± 2 K. In this investigation, fatigue failure life was defined as the number of cycles corresponding to 25% fall in the maximum tensile stress value at a given strain amplitude (Bhanu Sankara Rao et al. 1985). The fatigue crack initiation and propagation modes were characterized by examining the fracture surfaces and the longitudinal sections of the failed samples by optical microscopy and scanning electron microscopy (SEM). Energy dispersive analysis of X-rays (EDAX) was used to identify various carbides. The cyclic deformation-induced substructures were characterized by transmission electron microscopy (TEM). Samples for TEM examination were obtained from the thin slices sectioned at a distance of 1 mm away from the fracture surface. These slices were mechanically thinned down to 100 µm and 3 mm-diameter discs were punched. The discs were electropolished in a solution mixture containing 78% methanol, 10% lactic acid, 7% H_2SO_4, 3% HNO_3, 2%HF at 12 V and 240 K, in a twin-jet apparatus. TEM examination was carried out using Philips CM200 ATEM and FEI Tecnai G2 electron microscopes operating at 200 keV. Tensile tests were performed in the range 298–923 K at three strain rates (1.3×10^{-4} s^{-1}, 1.3×10^{-3} s^{-1}, 1.3×10^{-2} s^{-1}) and explored the effects of DSA during monotonic tensile deformation. The comparative assessment of monotonic and cyclic deformation at macroscopic level has been made.

Results

Initial Microstructure

The solution annealing at 1373 K/90 min dissolved a majority of the pre-existing (Ti, Mo)C and (TiC) particles and led to the complete dissolution of Chromium-rich $M_{23}C_6$ type of carbides and gamma-prime (γ'). Average grain size of Superni 263 alloy determined through linear intercept method was ~ 160 µm. Subsequent aging at 1073 K/8 h caused the re-precipitation of Cr-rich complex—$M_{23}C_6$ type of carbides on the grain boundaries (Fig. 1a, b) and uniformly distributed spherical γ' in the intragranular locations (Fig. 1c). The size distribution of γ' was large with an average size of 22 ± 4 nm (Fig. 1d).

The aging treatment at 1073 K for 8 h was found to give the peak yield and tensile strength when the alloy was subjected to different durations up to 48 h (Jadav 2019). The major inter-metallic precipitates in Alloy 263 at temperatures below 1173 K were reported to be γ' and η (Zhao et al. 2001; Crozeta and Devaux 2014). In this study, no η-phase was observed on ageing at 1073 K/8 h. It was reported that the η-phase would occur at the expense of the γ'-phase on prolonged annealing at 1073 K for durations exceeding ~ 3500 h (Zhao et al. 2001).

Effects of Temperature on Progressive Evolution of Cyclic Stress Response

The stress–strain hysteresis loops(SSHL) recorded at 473 K, 673 K, 773 K and 923 K are illustrated in (Fig. 2).

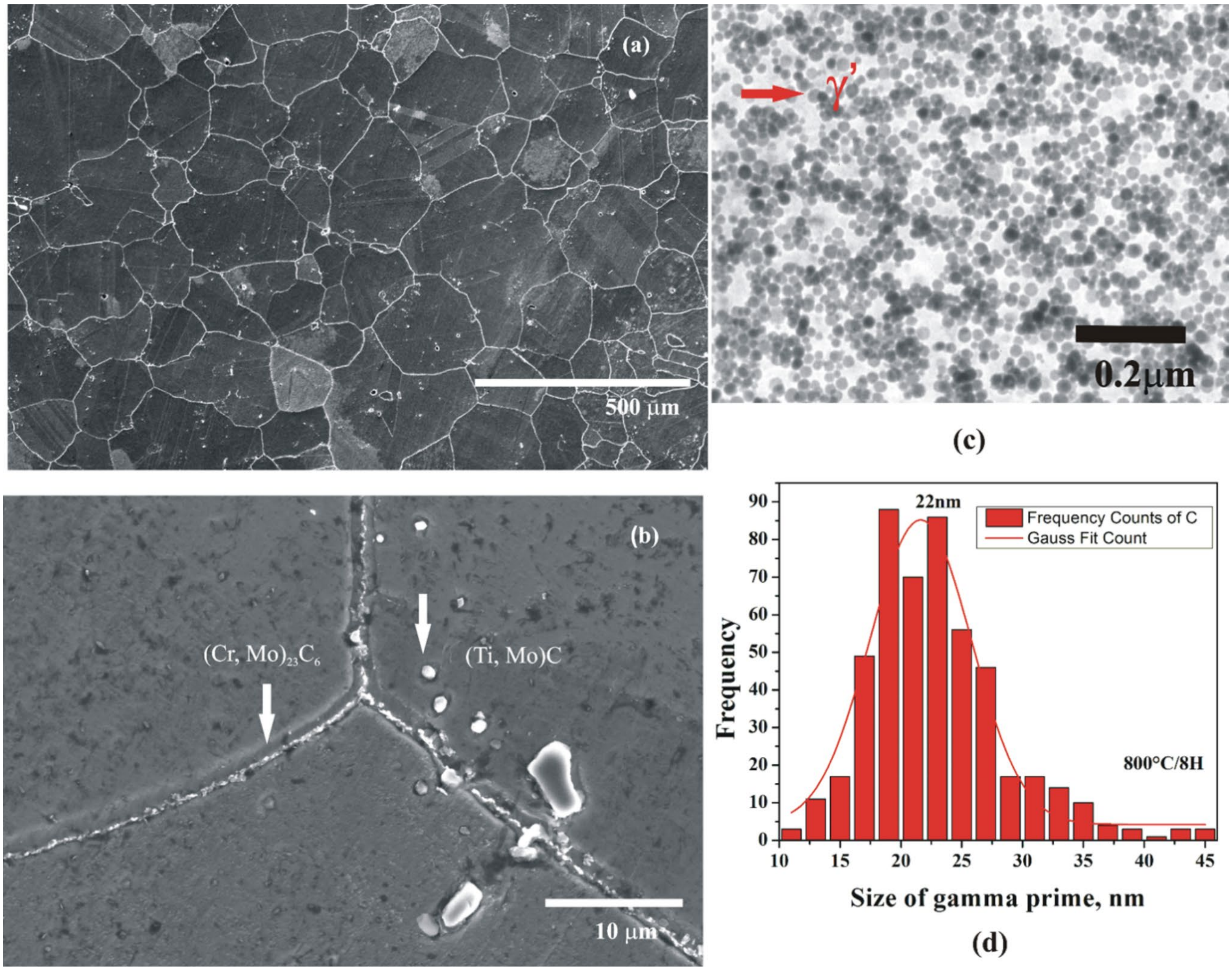

Fig. 1 Microstructure of the alloy in solution annealed plus aged condition: **a** SEM micrograph describing grain boundary carbide precipitation **b** SEM micrograph showing $M_{23}C_6$ precipitation on grain boundaries; blocky precipitates in the matrix were identified as (Ti, Mo) C **c** uniform distribution of spherical γ' in the matrix and **d** size distribution of γ' in the aged condition

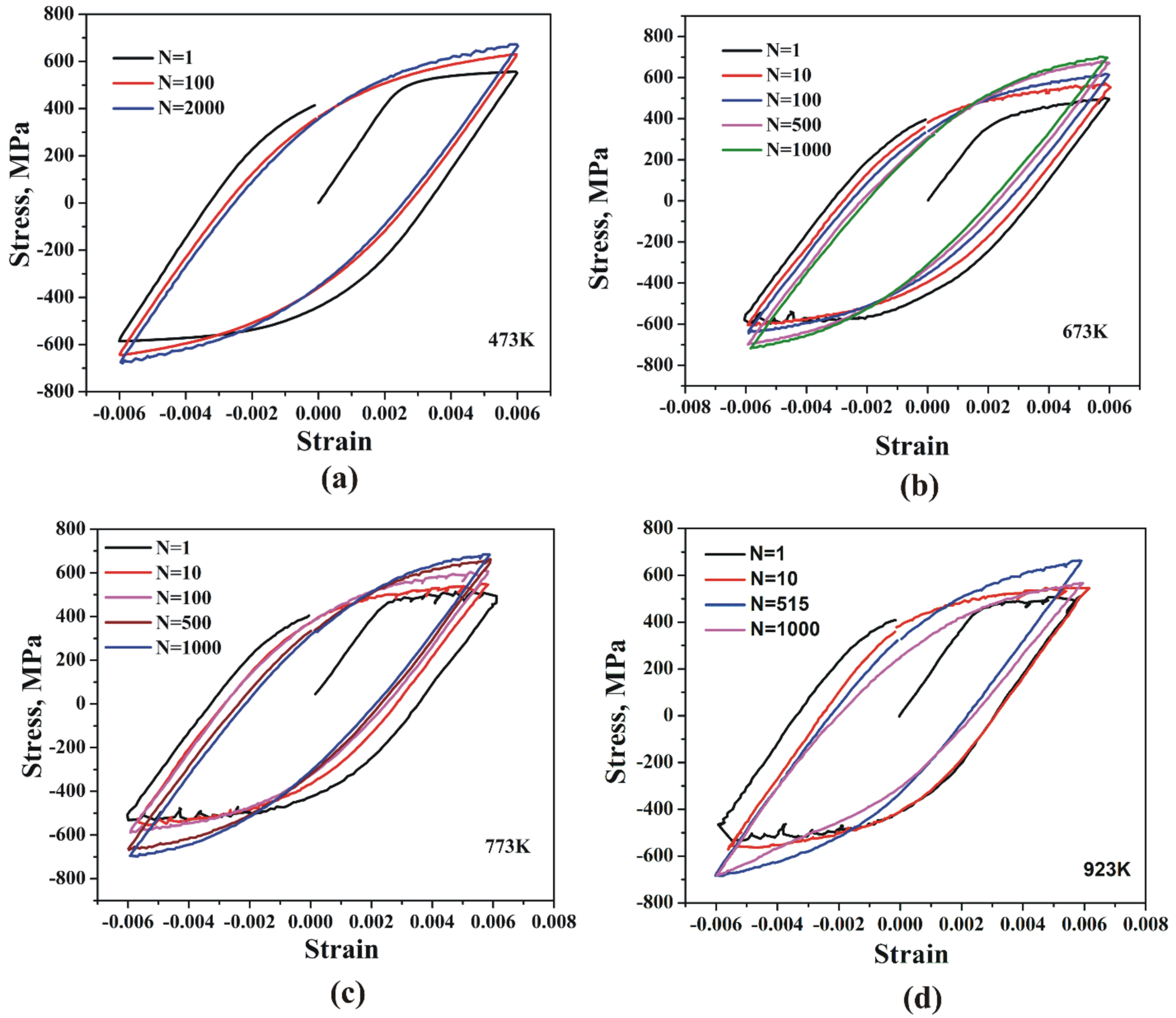

Fig. 2 Stress–strain hysteresis loops recorded at selected number of cycles at a strain amplitude of ± 0.60%, **a** 473 K **b** 673 K **c** 773 K and **d** 923 K. Plastic portions of stress–strain hysteresis loops depict the serrated flow observed at these temperatures

The hysteresis loops displayed serrations in the regions depicting plastic deformation between 473 and 1023 K. No serrated flow could be seen in the SSHLs in the tests performed at 298 K, and at 473 K the serrations appeared only after half-life (Fig. 2a). At temperatures higher than 573 K, the serrated flow started in the first quarter cycle as depicted in Fig. 2b–d and persisted till the end of fatigue life. The cyclic stress response (CSR) curves evolved as a function of temperature in the range 298–1023 K at a $\dot{\varepsilon}$ of $1 \times 10^{-3}\ \mathrm{s}^{-1}$ are shown in Fig. 3a, b. Based on the similarity in the cyclic stress response curves in Fig. 3a, b, the cyclic deformation behavior could be categorized broadly into three temperature domains. In the low-temperature domain below 473 K, the alloy underwent cyclic hardening in the first few cycles followed by slight softening. Towards the end, the tensile stress amplitude decreased at a faster rate as a consequence of initiation of microcracks and their growth. In the range between 573 K and 873 K, rapid cyclic hardening was observed and $\Delta\sigma/2_{\max}$ reached prior to the initiation of fatigue failure process. The number of cycles to attain the $\Delta\sigma/2_{\max}$ decreased with raising temperature in the intermediate temperature domain. The cyclic hardening was more prominent in the temperature interval between 573 and 673 K. In the high-temperature domain, at temperatures higher than 923 K, the alloy displayed a comparatively small period of cyclic hardening followed by a gradual cyclic softening stage that merged

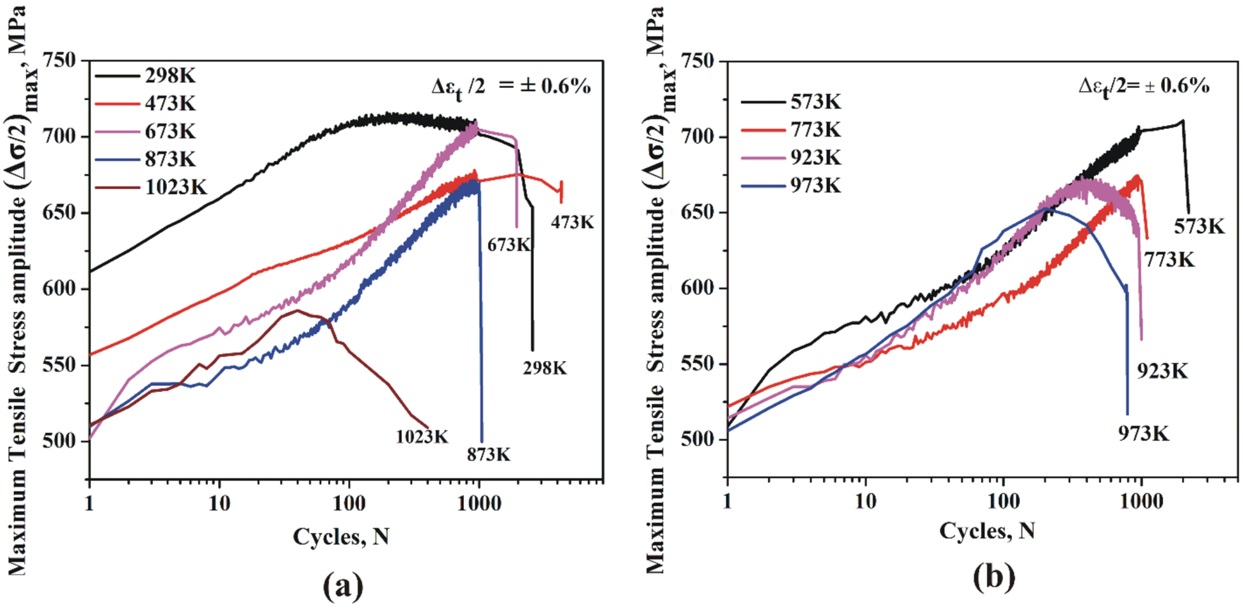

Fig. 3 **a** Cyclic stress response curves at a strain amplitude of ± 0.60% at 298 K, 473 K, 673 K, 873 K and 1023 K, **b** cyclic stress response curves at a strain amplitude of ± 0.60%, at 573 K, 773 K, 923 and 973 K

into microcrack initiation and propagation stages where the load-carrying capacity of the specimen was significantly declined.

The temperature dependence of LCF properties, such as the peak tensile stress amplitude, in the first quarter cycle ($\Delta\sigma/2_1$), the maximum tensile stress amplitude ($\Delta\sigma/2_{\max}$) developed during the total axial strain controlled LCF test, the stress amplitude pertaining to half of the failure life ($\Delta\sigma/2_{\mathrm{hl}}$), number of cycles to failure (N_{f}) and the inelastic strain amplitude developed in the cycle at half-life are summarized in Table 2.

Fatigue Crack Initiation and Propagation Modes and Fatigue Life

Temperature dependence of fatigue life revealed maximum at 473 K as shown in Fig. 4. In the domains encompassing intermediate and high temperatures, life decreased drastically with increasing temperature. Several important observations emerged on scrutinizing the fractured surfaces and the longitudinal cross sections of the failed specimens.

Irrespective of the temperature, fatigue cracks invariably initiated at the specimen surface (Fig. 5). Initially the crack propagation took place along the slip planes which were oriented at ~ 45° to the applied stress axis, at all test temperatures, designated as stage-I. Stage-I cracking persisted into

Table 2 Effect of temperature on LCF properties of Superni 263 superalloy with $\Delta\varepsilon_{\mathrm{t}}/2 = \pm 0.6\%$ and $\dot{\varepsilon} = 1 \times 10^{-3}\ \mathrm{s}^{-1}$

T (K)	N_{f} (cycles)	$(\Delta\sigma/2)_1$ (MPa)	$(\Delta\sigma/2)_{\mathrm{hl}}$ (MPa)	$(\Delta\sigma/2)_{\max}$ (MPa)	$(\Delta\varepsilon_{\mathrm{p}}/2)\%$ (half-life)
298	2600	611	702	714	0.27
473	4312	557	675	676	0.26
573	2748	509	710	710	0.23
673	1950	502	712	715	0.20
773	1470	522	688	691	0.22
873	1136	510	669	669	0.22
923	1030	514	665	665	0.22
973	790	506	642	654	0.24
1023	726	510	512	585	0.26

N_f represents no of cycles to failure at 25% drop in maximum tensile cyclic stress, $(\Delta\sigma/2)_1$ peak tensile stress amplitude in first cycle, $(\Delta\sigma/2)_{hl}$ half-life stress amplitude, $(\Delta\sigma/2)_{max}$ maximum stress amplitude, $(\Delta\varepsilon_p/2)\%$ inelastic strain amplitude at half-life

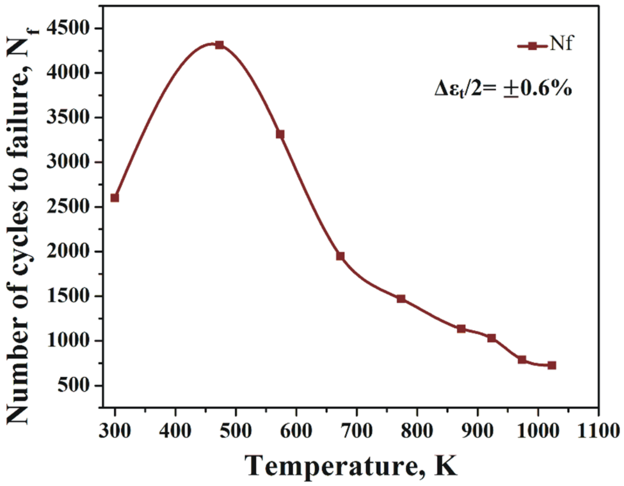

Fig. 4 Temperature dependence of fatigue life for Superni 263 superalloy at 10^{-3} s^{-1} (strain amplitude: ±0.60%)

one or two grains. The active slip planes of stage-I cracking were identified with cleavage facets (Fig. 5a, b). Stage II crack propagation commenced at the end of stage-I cracking and clearly displayed by signatures of striations on the fracture surface (Fig. 5c, d). Large number of micro cracks were noticed on the fracture surface of samples tested at 673 K (Fig. 5d), where the alloy exhibited maximum cyclic hardening.

In case of the specimens fatigued at 973 K and 1023 K, though the striations could be observed, the fracture surfaces were covered by thin adherent oxide layer (Fig. 6) indicating that the crack initiation and propagation probably was oxidation assisted. Despite the occurrence of oxidation, still the crack initiation took place by Stage-I mechanism at both 973 K and 1023 K (Fig. 5a).

Microscopic Deformation at Various Temperatures

In general, up to 873 K, the deformation majorly proceeded by planar slip in parallel slip bands (Fig. 7a) which possessed highest resolved shear stress. At 298 K, in some of the grains, cyclic deformation occurred by activation of {111} < 110 > and {100} < 110 > slip systems; the interaction of dislocations at the intersections of two slip planes led to formation of tangles that acted as barriers for further

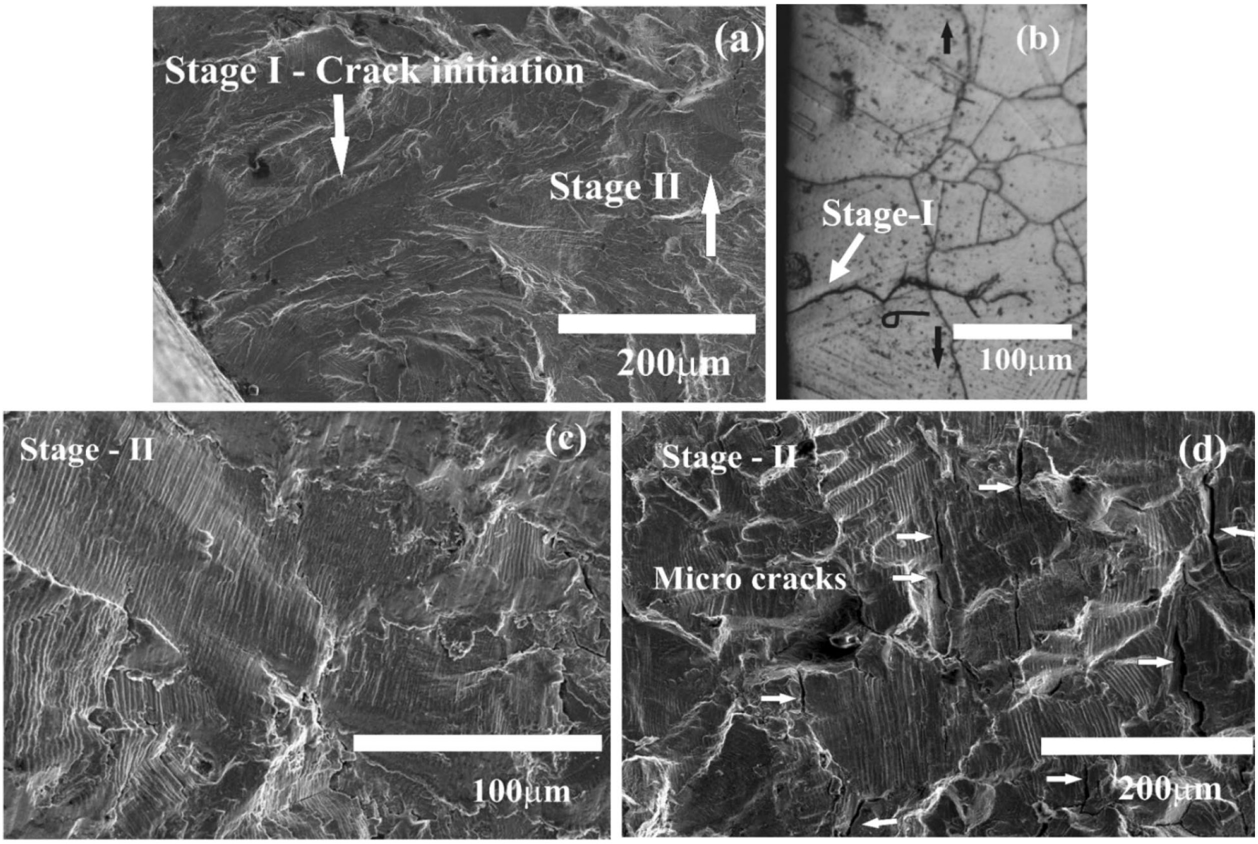

Fig. 5 **a** Stage I crack initiation at 1023 K depicting cleavage facets, **b** stage-I crack in transverse section of the sample tested at 923 K, striations on the fracture surface indicating stage II crack propagation at **c** 673 K and **d** 923 K. Large number of transgranular micro cracks are seen in the samples fractured at 673 K (indicated by arrows)

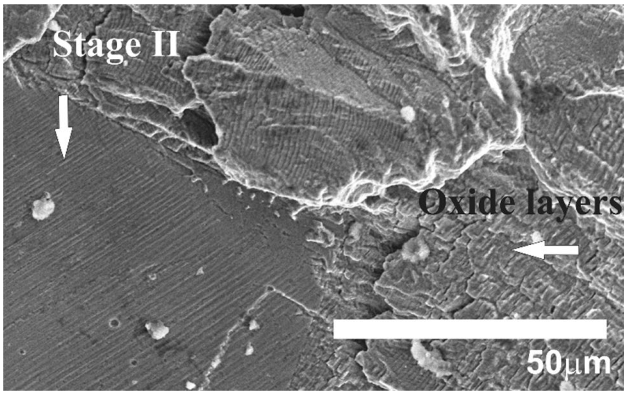

Fig. 6 Stage II crack propagation showing mildly oxidized surface at 973 K

dislocation movement (Fig. 7b). The planar slip bands exhibited individual dislocations, dislocation tangles, dislocation pairs as well as dislocation loops. The number density of slip bands revealed maximum at 673 K (Fig. 7c). Though few stacking faults were noticed at RT, the propensity for their formation was at its peak in the range 673–923 K. There has been intense interaction between γ' precipitates in slip bands/stacking faults as illustrated in Fig. 7d in this temperature range.

The plastic deformation in between the slip bands occasionally occurred by circumventing the coarse γ' precipitates initially present by the Orowan looping mechanism (Fig. 8a) below 923 K, whereas within the slip bands the γ' phase was often found sheared by dislocation movements (Fig. 8b). As a result, the γ' size became slightly finer within the slip bands. Figure 8c describes the occurrence of super lattice

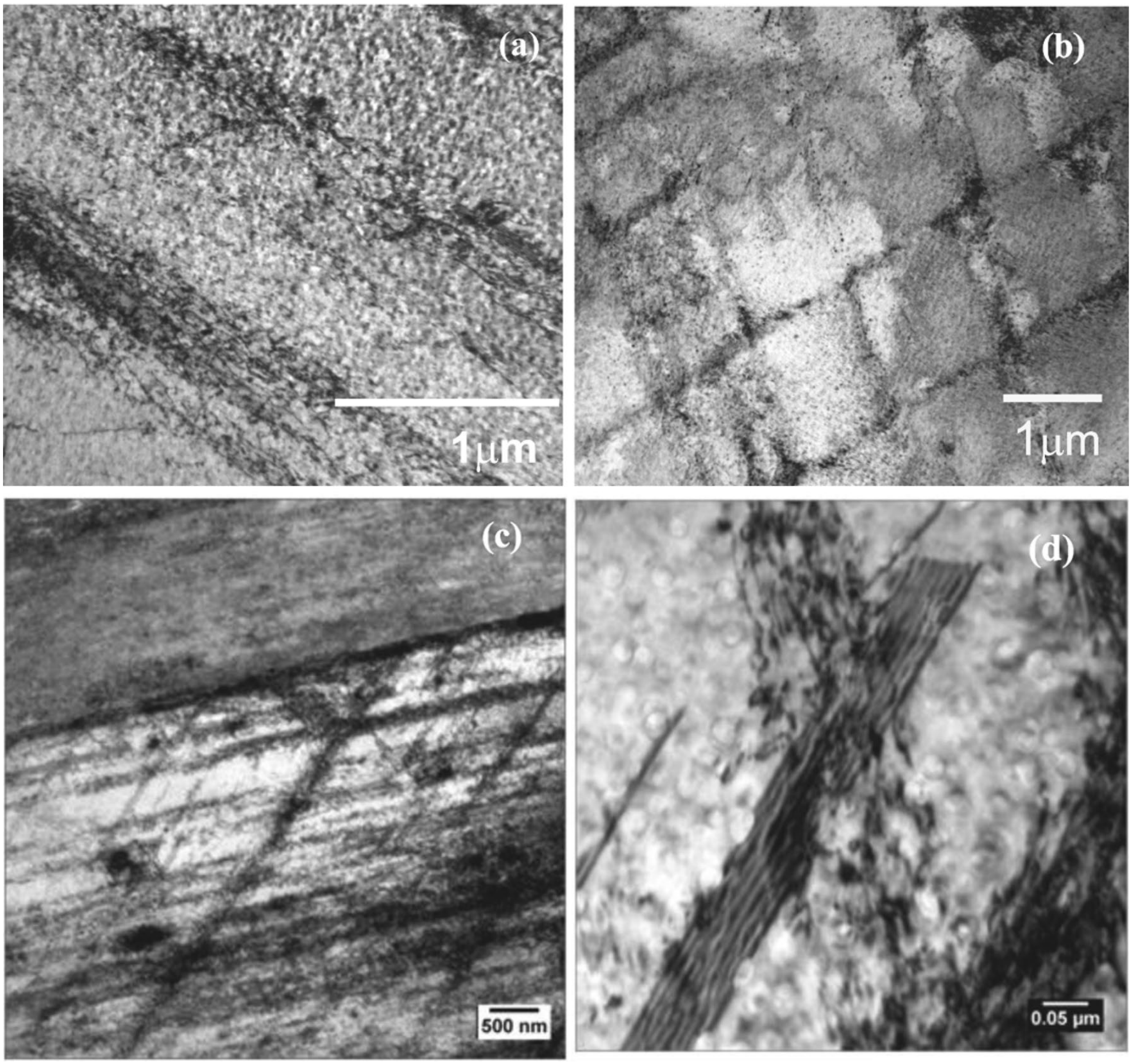

Fig. 7 Cyclic deformation in **a** parallel slip bands at 298 K and **b** deformation in two different slip systems showing dislocation tangles at the intersection of slip bands **c** high density of slip bands at 673 K, and **d** stacking fault fringes at 673 K

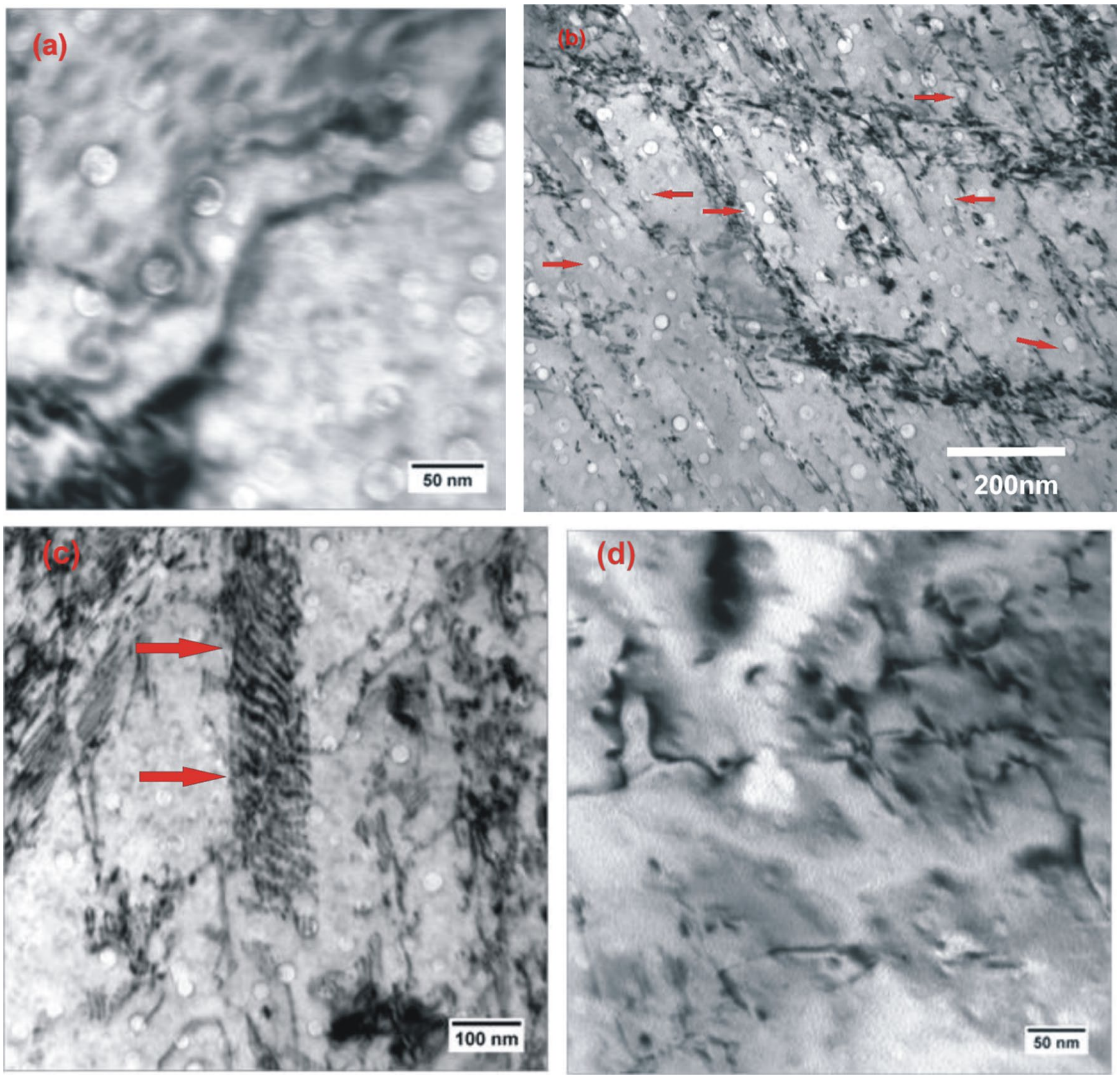

Fig. 8 **a** Looping of γ' particles in between the slip bands at 673 K **b** shearing of γ' precipitates within the slip bands which lead to small particle size, **c** super dislocation pairs in slip bands which provide evidence for γ' shearing at 673 K, and **d** predominant looping of γ' observed at 973 K and also displaying mottled contrast of the matrix giving an indication for very fine γ' precipitation during LCF deformation

dislocation pairs within a short slip band which serves as an evidence for γ' shearing. However, the alloy did not reveal any precipitation-free slip bands. At 923 K, some of the grains showed very high dislocation density in the configuration of networks. Above 973 K, the deformation proceeded predominantly by dislocation looping (Fig. 8d).

Cyclic Deformation Enabled Changes in Precipitation Behavior

Below 873 K, the γ' precipitate morphology remained spherical in the regions between slip bands, and no coarsening of the precipitates could be seen. At 923 K, few γ' particles were marginally coarsened. The morphology of the γ' in the edges of planar slip bands was elliptical (Fig. 9a); in fact, these elliptical shaped particles are two halves of sheared γ' particles. In the TEM evolution at 973 K, some of the grains exhibited mottled contrast probably due to fresh and very fine precipitation of γ' (Fig. 8d) during cyclic deformation. Figure 9b–d illustrate the bright field image, SAD pattern of γ and γ' precipitates along [100] zone axis and dark field image of γ' with (002) reflection, respectively.

After cyclic deformation at 973 and 1023 K, the grain boundary carbides remained discrete without any continuous carbide film formation. Figure 10a–c, respectively, describe BF image of $M_{23}C_6$ along grain boundaries, SAD pattern of γ and $M_{23}C_6$ along [− 112] zone axis and DF image of $M_{23}C_6$ with (220) reflection. LCF deformation at 1023 K led

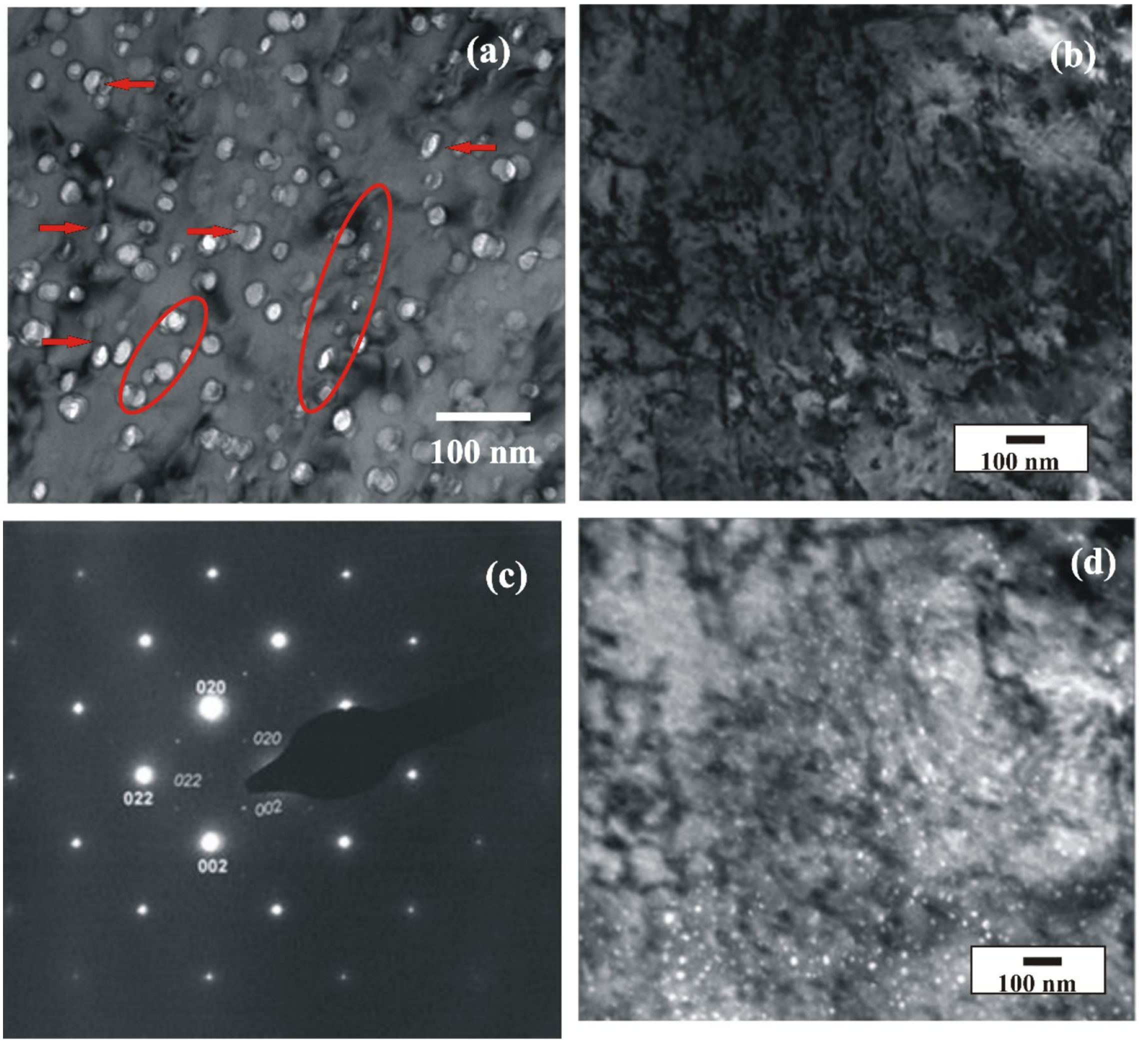

Fig. 9 **a** Morphology of γ' in the sample deformed at 923 K; elliptically shaped particles are two halves of sheared γ' particle; **b** illustrates the bright field image of γ' **c** SAD pattern of γ' and γ along [100] zone axis and **d** dark field image of γ' with (002) reflection

to partial recovery as depicted by incomplete cell formation, precipitation of very fine $M_{23}C_6$ in the intragranular regions of few grains on the dislocations introduced during cyclic deformation.

Discussion

Cyclic Stress Response, Serrated Flow and Dynamic Strain Ageing

In the low-temperature domain, the maximum tensile stress amplitude decreased initially with increasing temperature below 473 K, and increased with raise in temperature between 473 and 673 K displaying maximum at 673 K, and then decreased progressively beyond 773 K (Table 2). The temperature dependence of the half-life stress amplitude portrayed similar trends. The inelastic strain realized in a cycle at half-life decreased with increasing temperature up to 673 K, showing a minimum at 673 K. In the high-temperature domain (> 923 K), the inelastic strain generally increased with increasing temperature. In the intermediate-temperature domain, the negative temperature dependence of ($\Delta\sigma_{max}/2$), half-life stress amplitude and inelastic strain were attributed to the occurrence of dynamic strain ageing (DSA). In addition to these attributes, few more features were observed in this study, which elucidate the occurrence of DSA. In the tests performed between 573 and 1023 K, the alloy portrayed serrations in stress–strain hysteresis loops from first cycle onwards to the end of life (Fig. 2). In addition, the maximum rate of cycling hardening occurred at 673 K with minimum in the $\Delta\varepsilon_p/2$ corresponding to the cycle at half-life (Table 2). These observations serve as pointers to describe that the effects of DSA are maximum at

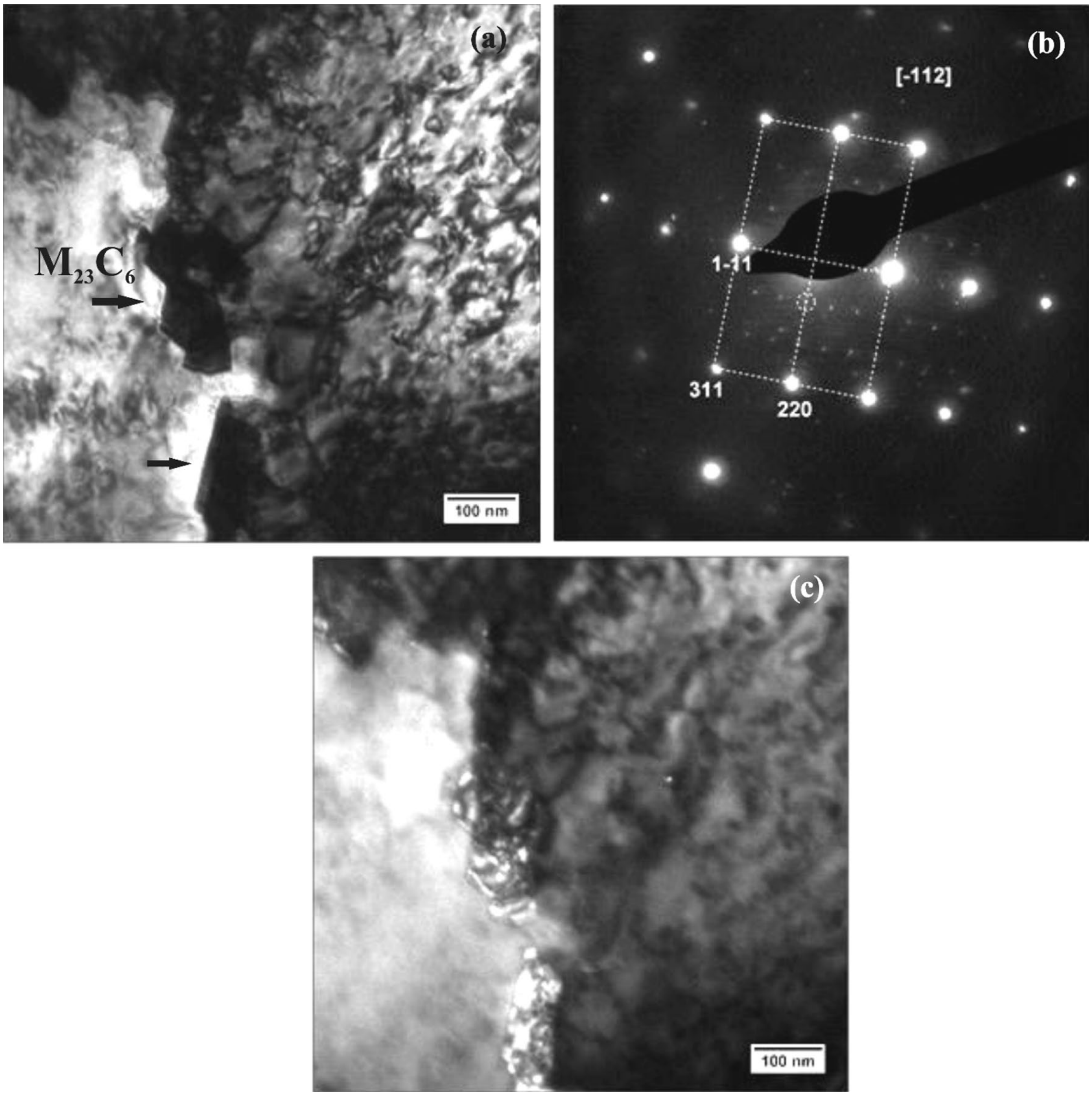

Fig. 10 **a** Bright field image of $M_{23}C_6$ along grain boundaries at 973 K **b** SAD pattern of γ and $M_{23}C_6$ along [− 112] zone axis **c** diffraction image of $M_{23}C_6$ with (220) reflection

673 K during LCF. During isothermal LCF tests, in the DSA domain, it has been shown that negative strain rate sensitivity manifests through an increase in half-life or peak stress amplitudes with decrease in $\acute{\varepsilon}$ in several stainless steels and superalloys (Srinivasan et al. 1991; Bhanu Sankara Rao 1989; Bhanu Sankara Rao et al. 1988a, 1990, 1991, 1997; Sandhya et al. 2005; Prasada Reddy et al. 2014; Valsan et al. 1992, 1994; Mariappan et al. 2016). In this investigation, the effects of $\acute{\varepsilon}$ on LCF behaviour have not been examined, but the strain rate dependence of flow behaviour during monotonic tension tests has been explored at various temperatures. The results from the tensile tests conducted from 298 to 923 K with different strain rates are compiled in Fig. 11.

At 298 K, the monotonic tensile flow stress decreased with decreasing $\dot{\varepsilon}$ in the range 10^{-2} s^{-1} to 10^{-4} s^{-1} indicating the positive SRS (Fig. 11a). In the range between 573 K and 923 K, the alloy exhibited an increase in the flow stress on decreasing the strain rate from 10^{-2} s^{-1} to 10^{-3} s^{-1} establishing the negative strain rate sensitivity (Fig. 11b–d). On further decreasing the $\dot{\varepsilon}$ from 10^{-3} s^{-1} to 10^{-4} s^{-1} the monotonic tensile flow stress decreased. These results suggest the operation of DSA is more prominent in the range 573–923 K, as supported by the prevalence of negative SRS. It must be pointed out that the temperature range in which serrated flow persisted (573–1023 K) was much broader than that of the DSA (573–923 K) regime.

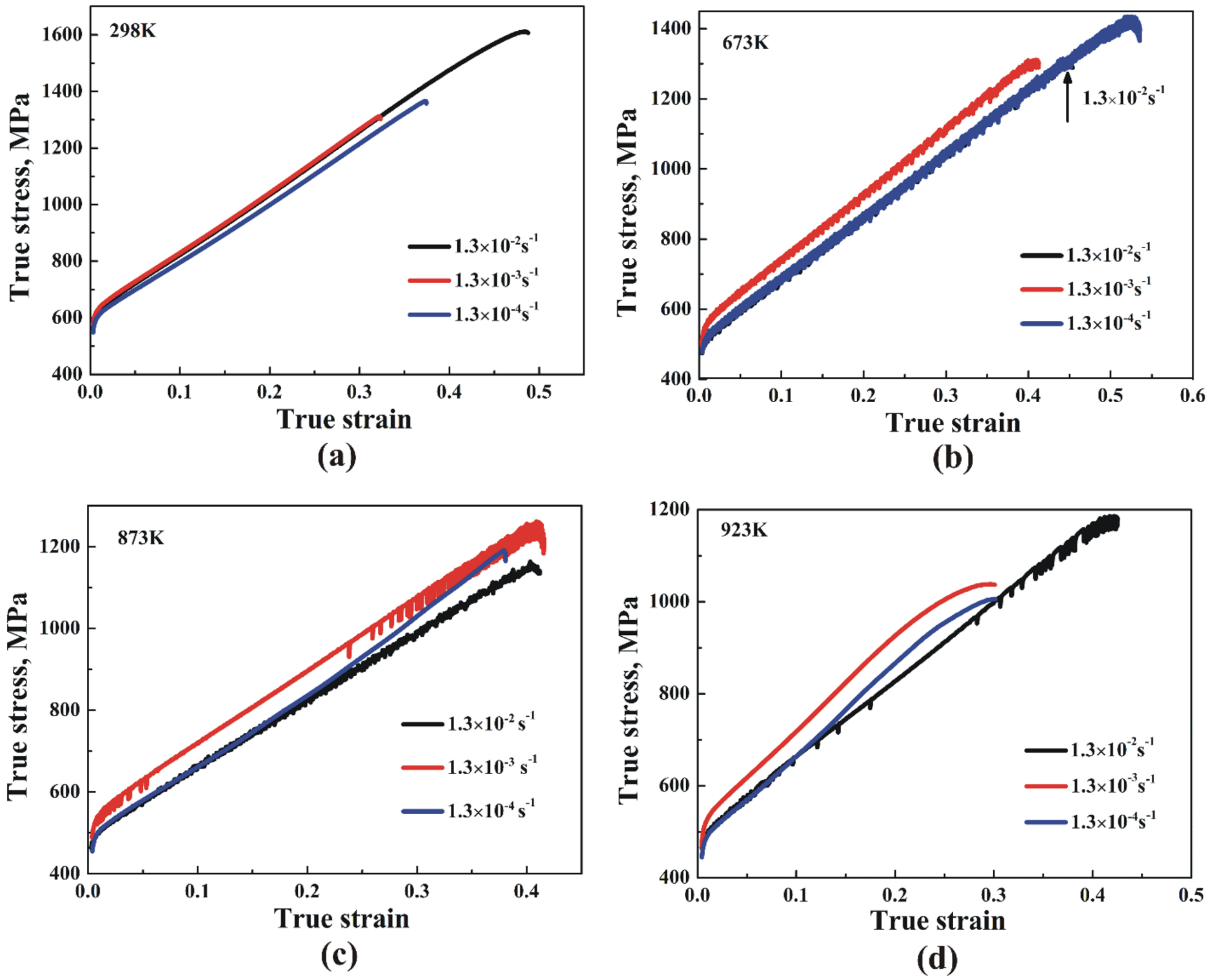

Fig. 11 True tensile stress–strain curves as a function of strain rate at **a** 298 K **b** 673 K **c** 873 K and **d** 923 K. The alloy shows positive strain rate sensitivity at 298 K but exhibits negative strain rate sensitivity of tensile flow stress in the DSA domain, 573–923 K

Dynamic strain ageing is generally considered to result from the interactions of mobile dislocations and diffusing solute atoms of different nature depending on temperature. It was proposed that ageing of mobile dislocations by solute atmospheres can occur either during quasi viscous-type dislocation motion (Cottrell 1953) or during the period when the dislocations were temporarily arrested at local obstacles in the slip planes (Van den Beukel and Kocks 1982; Van den Beukel 1980). An attempt has been made to assess the underlying mechanism of DSA. Different types of serrations that occurred during monotonic tensile deformation as a function of temperature at a $\dot{\varepsilon}$ of 10^{-3} s^{-1} in Superni 263 alloy are shown in Fig. 12. The serrations could be identified as per the classification proposed by (Rodriguez 1984). The type-A serrations characterized by an abrupt rise in stress followed by a drop to or below the general level of stress amplitude- total strain curve occurred at 573 K. Type-B serrations that describe the fluctuations around the general level

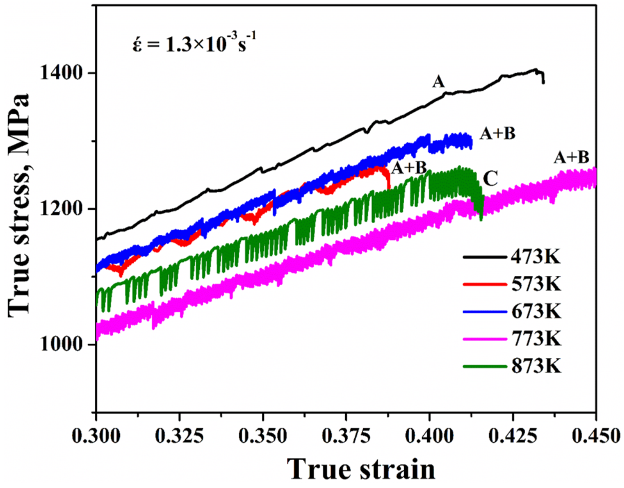

Fig. 12 Depicts Type-A and A + B serrations in the range 473–773 K and Type-C serrations at 873 K in monotonic tensile tests

of stress–strain curve and which occur in rapid succession were present between 473 and 773 K. Type-C serrations that fall below the stress–strain curve occurred at and above 873 K. Type A/B serrations are considered to result from the pinning of dislocations by solute atoms while type-C serrations represent the unlocking of dislocations from solute atmosphere. As illustrated in Fig. 2, all the serrations appeared after a certain amount of ε_c (critical strain) in the first quarter cycle. In the temperature range where type A/B serrations appeared the critical strain decreased with increasing temperature which was reported to be normal behavior. The critical strain value increased with increasing temperature in the zone pertaining to type-C serrations. The types of serrations that were seen in LCF tests (Fig. 2) are analogous to those observed in monotonic tensile tests at a given temperature (Fig. 12).

Based on the ε_c measurements in the temperature regime where type A/B serrations prevailed, the activation energy for the onset of serrated flow in monotonic tension tests was evaluated to be 68–77 kJ/mol (Jadav 2019); which are in agreement with that reported by Han et al. (2015) in Alloy 263. Since the first quarter cycle in LCF test in this study represents the tensile test up to 0.60% total strain, the observations made during tensile deformation can also remain valid for LCF tests. The pipe diffusion of substitutional atoms like Cr and Mo to dislocations in Ni-austenitic matrix has been suggested to cause the serrated flow (Rodriguez 1984) in the temperature range where the type A and type A + B serrations occur.

The cyclic stress response is generally dependent upon the internal resistance of the alloy for motion of dislocations. The deformation substructure in the DSA domain (573–773 K) consisted of high density of planar slip bands with narrower band spacing as shown in (Fig. 7c), high density of dislocations within the bands, and shearing of γ' precipitates which resulted in the reduction in the size of γ' particles (Fig. 8b). Many investigators established correlations between high work-hardening rates during tensile deformation and DSA in Nimonic PE 16 superalloy and austenitic stainless steels (Bhanu Sankara Rao 1989; Bhanu Sankara Rao et al. 1986). The higher work hardening rates in the DSA regime were shown to result from the increased rate of accumulation of dislocations (Sandhya et al. 2005). A number of dislocation pairs were noticed in the matrix as illustrated in Fig. 8b, c. Presence of dislocation pairs is considered as an evidence for shearing of ordered γ' particles by moving dislocations (Mariappan et al. 2016). In the regions between the slip bands, the spherical morphology of γ' particles was maintained below 873 K and the coarse particles were circumvented by the Orowan looping mechanism. In case of the superalloys undergoing shearing of γ', the strengthening predominantly results from two factors, coherency strain hardening and order hardening (Nembach 1981). The other phenomena such as modulus mismatch, flow stress mismatch and chemical hardening are considered negligible. In Alloy 263, like in Nimonic PE 16 Superalloy which exhibits spherical γ', the contribution to overall strengthening from coherency strains can also be considered very minor due to small-value of lattice mismatch between of γ' and of γ (Mariappan et al. 2016). Therefore, the cyclic hardening recorded initially, in the DSA regime, could be ascribed to the joint effects of order hardening associated with γ' shearing and work hardening resulting from pinning of the dislocations by solute atmospheres and dislocation–dislocation interactions.

At temperatures higher than 873 K, cyclic deformation was represented by initial hardening succeeded by cyclic softening, as illustrated in Fig. 3. The rapid fall in stress towards the end of life results from the initiation of micro-cracks, their growth and coalescence. This type of cyclic deformation behaviour has also been observed in other Ni-base superalloys (Bhanu Sankara Rao et al. 1988a; Mariappan et al. 2016; Nembach 1981; Merrik 1974; Stolz and Pineau 1978; Lerch and Gerold 1987; Fourier and Pineau 1977) and was ascribed either due to disordering of γ' due to mechanical scrambling or size reduction of γ' due to frequent shearing. Mechanical scrambling of the precipitates during LCF of WASPALOY is considered to result from the disordering of the fine precipitates of γ' by jogged dislocations (Stolz and Pineau 1978). The pathways of these jogs during back and forth motion cannot be reproduced and, therefore, results in mechanical scrambling of the γ', demolishing its order (Sundararaman et al. 1990). The cyclic softening in a Al–Cu alloy containing theta prime has been attributed to the disordering mechanism (Calabrese and Laird 1974), while the reduction in size of the γ' precipitates has been advanced to explain cyclic softening in Nimonic PE16 (Valsan et al. 1992) and Nimonic 80A (Lerch and Gerold 1987). The results obtained in the current investigation point out that the reduction in size of the γ' particles within the planar slip bands during repeated cyclic deformation below 873 K, and the coarsening of γ' particles at and above 923 K could probably be associated with gradual cyclic softening. Ripening of γ' precipitates decreases the tendency for the occurrence of DSA beyond 923 K. Coarsening of γ' has not been reported under stress-free thermal exposure in Alloy C263 at temperatures below 1023 K (Zhang and Knowles 2001). Deformation during LCF enables the coarsening of γ' to progress quickly due to the increased diffusion of solute elements that constitute the γ' precipitates such as aluminum and titanium. The rapid diffusion of these elements will be aided by the cyclic deformation-induced non-equilibrium vacancies. Fully reversed straining generates vacancies at a faster rate than stress-free thermal exposure at high temperatures (Essman and Mughrabi 1979; Antonovich 1981). Severe strain localization was reported to occur in the very fine γ'' hardened superalloys such as Inconel 718 (Bhanu Sankara Rao et al. 1994). Precipitation-free slip bands were shown to develop due to strain localization. It shall be mentioned that cyclic deformation-induced γ' precipitate-free channels and the dislocation pile-ups at the intersection of slip band and grain boundaries which promote intergranular cracks have not been observed in Superni 263 in the temperature range examined. In the solution-annealed state, the cyclic softening observed in several stainless steels (Srinivasan et al. 1991; Bhanu Sankara Rao et al. 1990, 1991, 1997) has been shown to result from the rearrangement of fatigue-induced dislocations into the configuration of cells, resulting in a larger mean free path for dislocations and a net decrease in dislocation density. In this investigation, Alloy 263 has not displayed either cells or sub-grains during the cyclic deformation in the range 298–923 K. The early signs of recovery in the form of cells have been seen occasionally in few grains in the tests conducted at 973 K and 1023 K. Furthermore, the fatigue-tested samples revealed additional precipitation of γ' at 973 K and 1023 K; these freshly formed precipitates are very fine and could be discerned from the mottled contrast (Fig. 8d) present in the thin foils of TEM. These fine precipitates would also get sheared and contribute to cyclic softening. The repeated shearing of γ' precipitates by dislocations moving in the same slip plane has been suggested to promote serrated yielding in the Udimet-520 superalloy (Doi and Shimanuki 1972). The nucleation of fresh γ' at temperatures lower than 973 K during isothermal exposure in Alloy 263 has not been reported, and, therefore, it would be expected that the interfacial diffusion Ti and Al atoms ensure the growth of γ' at less than 973 K.

The normalized cyclic stress response curves (peak tensile stress in successive cycles/first cycle peak tensile stress) are presented in Fig. 13. The normalized cyclic hardening values for several solid solution hardened alloys at peak DSA temperature are presented in Table 3. Though the precipitation strengthened Superni263 exhibits a higher ratio of the normalized cyclic hardening in its temperature dependence at peak DSA temperature of 673 K (Fig. 13), the hardening achieved by solid solution hardened stainless steels and solid solution strengthened superalloys was much greater at the respective peak DSA temperatures reported (Table 3).

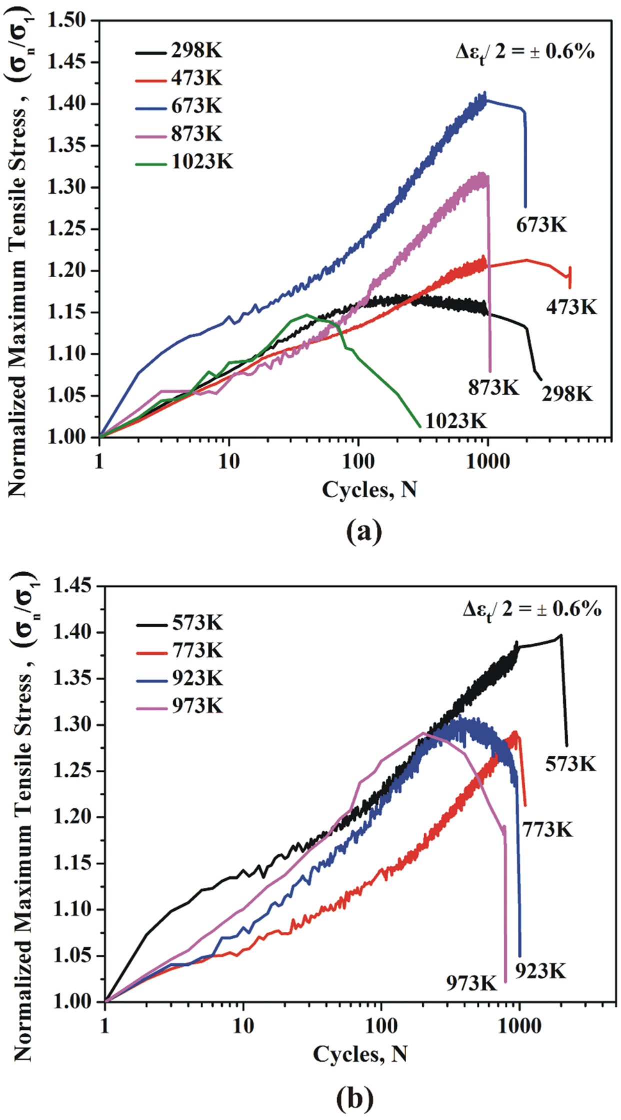

Fig. 13 **a** Normalized stress (peak stress in successive cycles/first cycle stress) response curves at 298 K, 473 K, 673 K, 873 K and 1023 K. **b** Normalized stress response curves at 573 K, 773 K, 923 K and 973 K

During DSA, the materials will uninterruptedly generate new dislocations to sustain the required mobile dislocation density at the imposed strain rate during the LCF testing (Bhanu Sankara Rao et al. 1997). This would occur because the ageing of mobile dislocations by solute atmospheres would result in impediment of dislocation motion. The interrupted LCF tests performed on solid solution hardened HASTELLOY X (Miner and Castelli 1992; Gopinath et al. 2009) revealed a progressive and considerable increase in dislocation density over a greater number of cycles in the DSA temperature range compared to that with room temperature. An increase in the dislocation density at failure on increasing the temperature from 473 to 873 K has also been observed (Gopinath et al. 2009). In solid solution hardened HAYNES 188 superalloy, the substructure in the DSA domain was accompanied by the formation of extensive planar slip, stacking faults, very high dislocation density and precipitation of very fine $M_{23}C_6$ particles on dislocations (Bhanu Sankara Rao et al. 1997). The substructure in the DSA range in the current investigation also showed some of these features.

During tensile deformation of γ' hardened Ni-base superalloys containing varying amounts of cobalt, it was noticed that the deformation mode changes from dislocation glide

Table 3 Normalized cyclic hardening values of many solid solution hardened alloys at peak DSA temperature

Alloy	Condition of the alloy	Strain amplitude	Strain rate, $\dot{\varepsilon}$, s^{-1}, ×10^{-3}	Testing temperature, K	DSA-temperature range, K	Peak DSA, K	Stress ratio, at peak DSA temperature, (σ_{max}/σ_1)
316L(N) (Srinivasan et al. 1991)	SA*	± 0.60%.	3	298–873	773–873	873	2.0
Alloy D9 (Sandhya et al. 2005)	SA	± 0.50%.	3	300–923 (Ti/C ratio = 8)	748–923	748 923	2.20 2.50
				(Ti/C ratio = 4)	673–823	823	2.80
316LN SS (0.14%N) (Prasada Reddy et al. 2014)	SA	± 0.6%	3	300–873	673–873	873	2.11
Haynes 188 (Bhanu Sankara Rao et al. 1997)	SA	± 0.4%	1	300–1273	573–1023	923	2.20
617 (Bhanu Sankara Rao et al. 1988a)	SA	± 0.3%	4	1023–1223	1123	1123	1.30
617 M (Shankar et al. 2017)	SA	± 0.6%	3	300–973	573–973	773	2.13
720Li (Gopinath et al. 2009)	Precipitation strengthened	> ± 0.6%	5	298–873	673	673	1.04

to SF formation with an associated switch in serrations from type A to type C (Cai et al. 2017). In case of Haynes 188, the entire grain was filled with stacking faults at 823 K, where type C serrations were found to exist (Bhanu Sankara Rao et al. 1995, 1997). Bhanu Sankara Rao et al. (1995) found that the SF density reaches a maximum and the SFE attains minimum in the inverse DSA regime in the Ni-base superalloys. These observations point out that the very high density of stacking faults occurs in the temperature range where the inverse DSA effect is predominant. Xu et al. (2014) expressed that DSA in a Co–Ni based superalloy is due to the interactions between the solute atoms and stacking faults. DSA studies in MP159 superalloy by Chiba and Kim (2001) employing field emission gun TEM revealed the Suzuki segregations around stacking faults (Han et al. 2003), which also has been found to correlate with the occurrence of serrated plastic flow in the range 723–943 K. It appears that the cyclic stress response in Superni263 was influenced by the competitive influence of DSA and shearing of γ' precipitates. Because of this, in Superni263, the normalized cyclic hardening peak values in the DSA range appears to be much smaller.

Correlation Between Fatigue Life and Fracture

The LCF life of the alloy was found maximum at 473 K and decreased rapidly with increasing temperature beyond 473 K (Fig. 4). This type of temperature dependence on fatigue life has also been exhibited by several austenitic stainless steels and superalloys (Crozeta and Devaux 2014; Srinivasan et al. 1991; Bhanu Sankara Rao et al. 1991; Sandhya et al. 2005; Valsan et al. 1994). At room temperature, the higher cyclic stresses developed cause the shortening of both transgranular crack initiation and propagation phases leading to lower life. The reduction in life at elevated temperatures in superalloys and stainless steels was attributed to factors like the enhanced magnitude of tensile inelastic strain in a given cycle, damage due to oxidation, and intergranular creep damage depicted by wedge cracks or cavities. In this investigation, Superni263 alloy exhibited a rapid decrease in life with increasing temperature despite minimum in inelastic strain was recorded at intermediate temperatures. In the intermediate temperature domain that extended from 573 to 923 K, the high cyclic response stresses developed due to DSA (Fig. 4) lead to an enhanced crack growth rate due to high stress concentration at the crack tip, with an associated reduction in the number of cycles to fatigue failure. Higher response stresses were also credited with a shortening of the critical crack size for final fracture (Bressers and Verheghee 1981; Bessers et al. 1986). DSA has been shown to cause early crack initiation and also promote an increase in the density of micro-cracks during the progression of the LCF test in Alloy 800H (Bessers et al. 1986). At the peak DSA temperature of 673 K, the Superni 263 superalloy has also displayed and a high number of transgranular micro-cracks as shown in Fig. 7c. The reduction in life above the DSA domain results from the combined effects of increased inelastic strain at half-life (Table 2) and deleterious effects of oxidation prevailing on the crack initiation and propagation stages. The mild oxidation observed on fracture surfaces of the LCF tested samples at 973 and 1023 K act as an indicator for the interference of the oxidation process in fatigue (Fig. 6). A comparative study conducted on 316L SS in air and vacuum at elevated temperatures revealed a faster rate of reduction in fatigue life in air due to rapid initiation of stage I transgranular cracks aided by oxidation (Driver et al. 1988). At high temperatures when transgranular fracture was predominant, it was shown that oxygen will either diffuse along slip bands to enhance stage-I cracking or ahead of the crack tip to enhance stage-II type of crack growth (Fujita 1958). Besides the enhancement of crack nucleation, oxidation also speeds up the growth rate of microcracks by enhancing the growth rate of individual cracks as well as through multiple crack coalescence (Bressers et al. 1987). The multiple crack coalescence observed in this investigation in the LCF test performed at 1023 K is illustrated in (Fig. 14a).

In this investigation, the fractographic studies conducted on crack propagation path (Fig. 14b) and the screening of longitudinal sections of LCF tested samples at 973 K and 1023 K did not reveal the creep damage that occurs in the form of either intergranular cracks or cavities. The intergranular $M_{23}C_6$ carbides present initially (Fig. 2b) seem to prevent the operation of grain boundary sliding and associated development of intergranular cracks or cavities. Furthermore, it has been noticed that there were no grain boundary carbide films that could trigger brittle intergranular cracking. It must be pointed out the fully reversed strain–time waveforms employed in this study are not conducive to develop the creep damage. Several studies have indicated that creep damage results in cycles comprising of dwell at peak strain in tension and or in cycles containing slow tensile going ramps and fast compressive going ramps (slow-fast cycles) (Rodriguez and Bhanu Sankara Rao 1993; Bhanu Sankara Rao et al. 1988b, 1996).

Conclusions

- The cyclic stress response of the alloy was dictated by the temperature of testing. Based on the macroscopic cyclic stress response, three temperature regimes were identified. At temperatures lower than 473 K, the Superni263 displayed a very brief period of cyclic hardening and reached a saturation stress period in the early stages of fatigue life. Toward the later stage of LCF tests, the $\Delta\sigma/2$ declined rapidly due to the initiation and growth of micro-cracks. Rapid cyclic hardening has occurred in the intermediate temperature domain spread over 523–923 K until the onset of failure. The maximum cyclic hardening took place at 673 K. At and above 973 K, the alloy displayed a reduced degree of cyclic hardening in the initial stages compared to that in the DSA domain.
- The pronounced cyclic hardening occurred between 523 and 923 K has been attributed to DSA of dislocations. The DSA process exhibited several manifestations in its operating temperature range. Serrated flow occurred in the plastic deformation portions of hysteresis loops. Superni263 showed inverse temperature dependence of $\Delta\sigma_{max}/2$ and $\Delta\varepsilon_p/2$ developed at half of the LCF life. The ratios of peak stress to first cycle stress were found high at various temperatures in the DSA domain.
- The substructure evolved in the DSA range consisted of planar slip bands, stacking faults, dislocation tangles between the slip bands and dislocation-precipitate interactions.

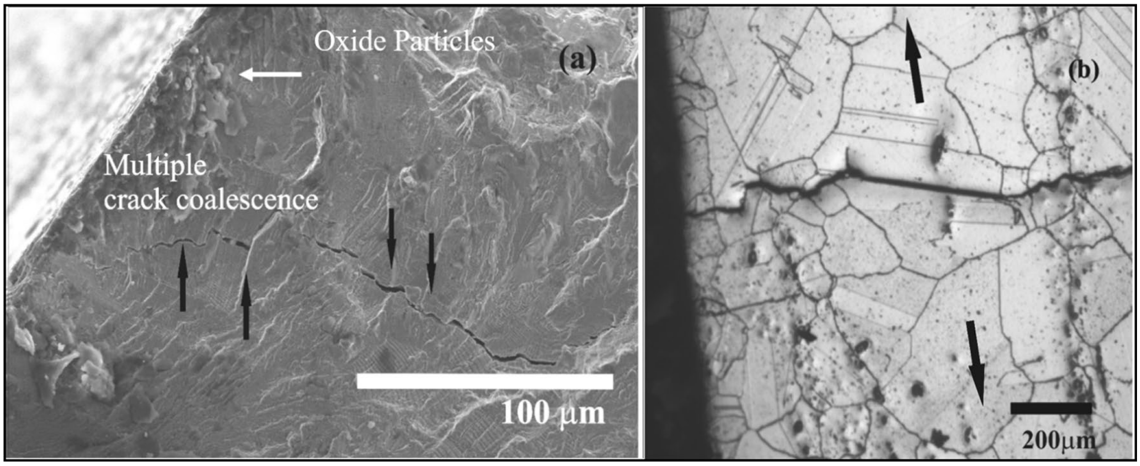

Fig. 14 **a** The fracture surface revealing oxide particles in the surface near regions and multiple crack coalescence in the samples tested at 1023 K and **b** transgranular crack propagation at 973 K in longitudinally sectioned samples without evidence for intergranular cavities and cracks due to creep

- In the range 673–923 K, Superni263 alloy has undergone shearing of fine γ' and looping of coarse γ' precipitates owing to the size distribution in the starting microstructure of the alloy. Though the shearing occurred in planar slip bands, the deformation was confined to very short lengths in the matrix. There were neither γ' particle-free bands in the matrix nor pile-up of dislocations in planar slip bands at intersections of the grain boundaries were seen.
- At and above 973 K, fresh precipitation of γ' within the matrix, and $M_{23}C_6$ on deformation-induced dislocations were noticed.
- The crack initiation and propagation at all the temperatures occurred in transgranular mode. No evidence for intergranular cracking was obtained.
- The alloy displayed maximum life at an intermediate temperature of 473 K. The lower life at 298 K resulted from the effects of a high cyclic stress response. In the intermediate temperature range encompassing 523–923 K, the drastic reduction in LCF life was attributed primarily o the detrimental effects of DSA. At and above 973 K, fatigue life reduction has been found to correlate with oxidation assisted fatigue crack initiation and propagation.

Acknowledgements Some of the experimental facilities used in these investigations are supported by DST-FIST program, DST-Centre for Nanotechnology at the University of Hyderabad, Hyderabad, India.

Compliance with Ethical Standards

Conflict of interest The authors declare that they have no competing interest

References

Antonovich S, Rosa D, Pineau A (1981) Low cycle fatigue of René 77 at elevated temperatures. Mater Sci Eng 47:47–57

Beukel A, Kocks UF (1982) The strain dependence of static and dynamic strain-aging. Acta Metall 30:1027–1034

Bhanu Sankara Rao K (1989) Influence of metallurgical variables on low cycle fatigue behavior of type 304 stainless steel-Grain size, cold work and thermal aging effects, Ph.D. thesis, University of Madras, India

Bhanu Sankara Rao K, Valsan M, Sandhya R, Ray SK, Mannan SL, Rodriguez P (1985) On the failure condition in low cycle fatigue. Int J Fat 7:7–12

Bhanu Sankara Rao K, Seetharaman V, Mannan SL, Rodriguez P (1986) Strain rate and temperature dependence of deformation and fracture behaviour of a Nimonic PE 16 superalloy. High Temp Mater Process 7:63–72

Bhanu Sankara Rao K, Schiffers H, Schuster H, Nickel H (1988a) Influence of time and temperature dependent processes on strain controlled low cycle fatigue behavior of Alloy 617. Metall Mater Trans A 19A:359–371

Bhanu Sankara Rao K, Meurer HP, Schuster H (1988b) Creep-fatigue interaction of inconel 617 at 950 C in simulated nuclear reactor helium. Mater Sci Eng 104:37–51

Bhanu Sankara Rao K, Valsan M, Sandhya R, Mannan SL, Rodriguez P (1990) Manifestations of dynamic strain aging during low cycle fatigue of Type 304 stainless steel. Metal Mater Proc 2:17–36

Bhanu Sankara Rao K, Valsan M, Sandhya R, Mannan SL, Rodriguez P (1991) Synergistic interactions during high temperature fatigue of type 304 stainless steel. Trans Ind Inst Metal 44:255–270

Bhanu Sankara Rao K, Halford GR, McGaw MA (1994) In: Loria EA (ed) Proc. Third Intl Special Emphasis Sympo. on Superalloys 718, 625,706 and derivatives, Pittsburgh

Bhanu Sankara Rao K, Castelli MG, Ellis JR (1995) On the low cycle fatigue deformation of Haynes 188 superalloy in the dynamic strain aging regime. Scripta Metall Mater 33:1005–1012

Bhanu Sankara Rao K, Schuster H, Halford GR (1996) Mechanisms of high temperature fatigue failure in alloy 800H. Metall Mater Trans A 37A:851–861

Bhanu Sankara Rao K, Castelli MG, Allen GP, Ellis JR (1997) A critical assessment of the mechanistic aspects in Haynes 188 during low cycle fatigue in the range 25 °C to 1000 °C. Metall Mater Trans A 28A:347–361

Bhattachar VS (1995) Thermal fatigue behavior of nickel-base superalloy 263 sheets. Int J Fatigue 17:407–413

Bressers J, Verheghee (1981) The effect of time dependent-processes on the high temperature low cycle fatigue life of Waspalloy. Res Mech Lett 1:55–59

Bressers J, Remy L, Hoffelner W (1986) Fatigue dominated damage processes. In: Betz W et al (eds) Proc. conf. high temperature alloys for gas turbines and other applications, Leigh, 6–9 Oct 1986. D. Riedel Publishing Company, Dordrecht, p 441

Bressers J, Schusser U, Illschner B (1987) Low cycle fatigue and elasto-plastic behaviour of materials. In: Rie KT (ed) Elsevier Applied Science, London, pp 365–370

Cai Y, Tian C, Zhang G, Han G, Yang S, Fu S, Cui C, Zhang Q (2017) Influence of γ' precipitates on the critical strain and localized deformation of serrated flow in Ni-based superalloys. J Alloy Compd 690:707–715

Calabrese C, Laird C (1974) Cyclic stress-strain response of two-phase alloys Part I. Microstructures containing particles penetrable by dislocations. Mater Sci Eng 13:141–157

Chiba A, Kim MS (2001) Suzuki segregation and dislocation locking in supersaturated Co–Ni based alloy. Mater Trans 42:2112–2116

Cottrell AH (1953) A note on the Portevin-Le Chateliereffect. Philos Mag 44:829–835

Crozeta C, Devaux A, Bechet D (2014) Microstructure stability: optimisation of 263 Ni-based superalloy. MATEC Web Conf 14:17006. https://doi.org/10.1051/matecconf/20141417006c

Doi H, Shimanuki Y (1972) In: Proc. 2nd Intl. Conf. on superalloy processing, Champion. Metals and Ceramics Information Center, Columbus, Ohio

Driver JH, Gorlier C, Belrami C, Vidan P, Amzallag C (1988) Influence of temperature and environment on the fatigue mechanisms of single crystal and polycrystal . In: ASTM STP (American Society for Testing and Materials), pp 438–455

Essman U, Mughrabi H (1979) Annihilation of dislocations during tensile and cyclic deformation and limits of dislocations densities. Philos Mag A 40:731–756

Fourier D, Pineau E (1977) Low cycle fatigue behavior of Inconel 718 at 298 K and 823 K. Metall Trans A 8:1095–1105

Fujita FE (1958) Dislocation theory of fracture of crystals. Acta Metall 6:543–551

Gianfrancesco AD (2017) Materials for ultra-supercritical and advanced ultra-supercritical power plants, Chapter 17, Alloy 263. Elsevier Ltd., Amsterdam, pp 571–598

Gopinath K, Gogia AK, Kamat SV, Balamuralikrishnan R, Ramamurty U (2009) Low cycle fatigue behavior of a low interstitial Ni-base superalloy. Acta Mater 57:3450–3459

Han GW, Jones IP, Smallman RE (2003) Direct evidence for Suzuki segregation and Cottrell pinning in MP 159 superalloy obtained by FEG(S)TEM-EDX. Acta Mater 51:2731–2742

Han GM, Tian CG, Chu ZK, Cui CY, Hu ZQ, Sun XF (2015) Activation energy calculations for the Portvein-Le Chatlier effect in nimonic 263 superalloy. Metall Mater Trans A 46A:4629–4635

Jadav JB (2019) Assessment of precipitation, deformation and fracture behavior of Superni 263 Nickel-Base superalloy under tensile and low cycle fatigue conditions, Ph.D. Thesis, University of Hyderabad

Lerch BA, Gerold V (1987) Room temperature deformation mechanisms in Nimonic 80A. Metall Trans A 18A:2135–2141

Maile K (2013) Qualification of Ni-based alloys for advanced ultra-supercritical plants. Proc Eng 55:214–220

Mariappan K, Shankar V, Goyal S, Sandhya R, Laha K, Bhaduri AK (2016) Strain amplitude and temperature effects on the low cycle fatigue behavior of Alloy 617M. Trans Ind Inst Metals 69:325–329

Merrik HF (1974) The low cycle fatigue of three wrought nickel-base alloys. Metall Trans A 5:891–897

Miner RV, Castelli MG (1992) Hardening mechanisms in a dynamic strain aging alloy, HASTELLOY X, during isothermal and thermomechanical cyclic deformation. Metall Trans A 23A:551–561

Nembach E (1981) Hardening of Nimonic alloy PE 16 by ordered γ'-precipitates. Z Metallkd 72:401–405

Pohja R, Nurmela A, Holmstrom S, Moilanen P (2015) Creep-fatigue properties of nickel-base superalloy 263. VTT Technical Research Centre, Finland

Prasada Reddy GV, Sandhya R, Sankaran S, Mathew MD (2014) Low cycle fatigue behavior of 316LN stainless steel alloyed with varying nitrogen content: part I, cyclic deformation behavior. Metall Mater Trans A 45A:5044–5056

Ratna V, Sarma DS (1993) Influence of thermal fatigue on the microstructure of a Ni-base superalloy. Scripta Metallrgica et Materialia 29:467–472

Rodriguez P (1984) Serrated plastic flow. Bull Mater Sci 6:653–658

Rodriguez P, Bhanu Sankara Rao K (1993) Nucleation and growth of cracks and cavities under creep-fatigue interaction. Progr Mater Sci 37:403–480

Sahu JK, Ravikumar B, Das SK, Paulose N, Mannan SL (2015) Isothermal high temperature low cycle fatigue behavior of Nimonic 263: influence of Type I and Type II hot corrosion. Mater Sci Eng A 622:131–138

Sandhya R, Bhanu Sankara Rao K, Mannan SL (2005) Effect of Ti/C ratio on temperature dependence of low cycle fatigue behavior of 15Cr–15Ni titanium modified austenitic stainless steel. Mater Sci Technol 21:178–184

Shankar V, Kumar A, Mariappan K, Sandhya R, Laha K, Bhaduri AK, Narasaiah N (2017) Occurrence of dynamic strain aging in Alloy 617 M under low cycle fatigue loading. Int J Fatigue 100:12–20

Smith SA, West GD, Chi K, Gamble W, Thomson RC (2010) Advances in materials technology for fossil power plants. In: Proceedings from sixth international conference, pp 110–126

Srinivasan VS, Sandhya R, Bhanu Sankara Rao K, Mannan SL, Raghavan KS (1991) Effects of temperature on the low cycle fatigue behavior of nitrogen alloyed Type 316L stainless steel. Int J Fatigue 13:471–478

Stolz RE, Pineau A (1978) Dislocation-precipitate interaction and cyclic stress–strain behavior of a γ′ strengthened superalloy. Mater Sci Eng 34:275–284

Sundararaman M, Chen W, Singh V, Wahi RP (1990) TEM investigation of γ′ free bands in nimonic PE16 under LCF loading at room temperature. Acta Metall 38:1813–1822

Valsan M, Parameswaran P, Bhanu Sankara Rao K, Vijayalakshmi M, Mannan SL, Shastry DH (1992) High-temperature low-cycle fatigue behavior of a nimonic PE-16 superalloy—correlation with deformation and fracture. Metall Mater Trans A 23A:1751–1761

Valsan M, Shastry DH, Bhanu Sankara Rao K, Mannan SL (1994) Effect of strain rate on the high temperature low cycle fatigue properties of a Nimonic PE-16 superalloy. Metall Mater Trans A 25A:159–171

Van den Beukel A (1980) On the mechanism of serrated yielding and dynamic strain aging. Acta Metall 28:965–969

Xie XS, Dong JX, Wang J (2011) Structural stability analysis of Nimonic 263 after long term stress rupture tests (internal Report), High temperature materials research laboratories. University of Science and Technology, Beijing

Xu YJ, Qi DQ, Du K, Cui CY, Ye HQ (2014) Stacking fault effects on dynamic strain aging in a Ni–Co based superalloy. Scripta Mater 87:37–40

Zhang YH, Knowles DM (2000) Isothermal and thermomechanical fatigue of superalloy C-263, Superalloys 2000. In: Pollock TM, Kissinger RD, Bowman RR, Green KA, McLean M, Olson S, Schina TMS (eds) The Minerals, Metals and Materials Society

Zhang YH, Knowles D (2001) Micromechanisms of creep deformation of C263 superalloy, Interim Report 2/AT29, UTC, Department of Materials Science and Metallurgy, Cambridge University

Zhao JC, Ravikumar V, Beltran AM (2001) Phase precipitation and phase stability in Nimonic 263. Metall Mater Trans A 32A:1271–1282